

**The Characterization
of a 34-Meter Beam-Waveguide Antenna
at K_a-band (32.0 GHz) and X-band (8.4 GHz)**

**David D. Morabito
Jet Propulsion Laboratory
California Institute of Technology
Pasadena, California**

(Revised December 21, 1998)

ABSTRACT

New antennas for the NASA Deep Space Network (DSN) have been built to replace the aging antennas of older designs for deep space communications. These new antennas incorporate a new dual-shape design as well as a beam waveguide (BWG), which utilize a series of additional secondary mirrors to relocate the focal point into a stationary room below the main reflector. The advantages of using such a design include increased isolation of the feed package from outside environmental factors such as moisture, wind, and temperature changes and ease of access to the equipment for maintenance, troubleshooting and repair purposes.

This article reports on the performance of a beam waveguide antenna at X-band and Ka-band microwave frequencies. The K_a-band Antenna Performance Experiment (KaAP) antenna efficiency measurements presented in this article were acquired at the Goldstone DSS-13 Research and Development (R&D) beam waveguide (BWG) antenna between December 1993 and November 1995.

The measured antenna efficiency and ground station figure-of-merit (gain divided by operating system noise temperature) as a function of elevation angle and their uncertainties are presented. Also described are the station configuration, the measurement technique, the modeling used in the analysis processing, and the historical evolution of the DSS-13 K_a-band antenna efficiency measurements as progressive improvements and configuration changes were implemented.

1. INTRODUCTION

The Beam-WaveGuide (BWG) design feature had been in use for several years for communications satellite terminals where ease of service outweighed the added noise due to the additional mirrors. However, for NASA Deep Space Network (DSN) usage, the concern for the added noise initially kept such antennas out of contention. In 1985, a team of JPL researchers worked in collaboration with Japan's Institute for Space and Astronautic Sciences (ISAS) to install one of JPL's experimental low-noise amplifiers into the ISAS 64-m BWG antenna in Usuda, Japan. This configuration was demonstrated at S-band (2-GHz) using the International Cometary Explorer (ICE) spacecraft achieving good performance with no significant noise penalty. Moving from this demonstration to application of the BWG technology in the DSN resulted in the building of the prototype DSS-13 antenna. The completed antenna operated effectively at 2, 8, and 32 GHz [1].

Several DSN telecommunications studies have shown that by utilizing K_a -band (31.8 to 32.3 GHz) frequencies in place of X-band (8.40 to 8.45 GHz) on a spacecraft-to-ground communications link, an advantage of approximately 7 dB (factor of 5 improvement) can be realized for a given spacecraft transponder weight, antenna size and power allocation [2,3]. The link advantage can be used to increase data volume, decrease transmission time, decrease transmitter power on the spacecraft, decrease spacecraft antenna size, or allow for a smaller antenna on the ground. The increased advantage comes from increased antenna gain at the shorter wavelengths. However, in practice, the advantage is reduced by higher atmospheric noise, antenna performance deficiencies and weather susceptibility at K_a -band.

The concept of conducting a K_a -band link experiment to verify these studies and to discover any impediments that could deter this performance gain from being realized was proposed by Riley et al. 1987 [4]. The first K_a -band link experiment at 33.7 GHz became reality with the Mars Observer Project's KaBLE (Ka-Band Link Experiment) which acquired data at DSS-13 from Mars Observer's Ka-band beacon and X-band signal between January and August, 1993 [5].

With the loss of Mars Observer in August 1993, it became important to find other ways to continue the study of the link advantage until another spacecraft with Ka-band capability became available. The KaAP (K_a -band Antenna Performance Experiment) Project was initiated in December 1993 to evaluate antenna efficiency by observing natural radio sources at both Ka-band and X-band. These evaluations allow the characterization of the antenna efficiency at each frequency band as incremental performance improvements and configuration changes are realized. The ground station advantage of K_a -band relative to X-band is quantified using the acquired data from both bands. The effort also facilitates the demonstration and development of optimal operational strategies for BWG antennas. The information gained is of benefit to the DSN and flight projects which may be considering Ka-band for their telecommunications link carrier frequency. The knowledge gained about the temporal variability of the K_a -band advantage due to weather effects allows planners of future flight projects to develop robust, efficient telecommunication

strategies at Ka-band.

Since the loss of Mars Observer in 1993, Ka-band data have been acquired from two additional spacecraft. SURFSAT-1, launched on November 4, 1995, was a DSN Technology Program flight experiment. Surfsat-1 tracking data were acquired between launch in November 1995 and December 1996 for the purpose of characterizing this link advantage. Mars Global Surveyor, launched in November 1996, carries KaBLE-II, another DSN Technology Program experiment. MGS KaBLE-II Ka-band data are currently being acquired at DSS-13 and preliminary results have been published [6, 7]. These missions allow Ka-band link advantage studies to continue using X-band and Ka-band spacecraft signal sources. In October 1998, another spacecraft with Ka-band capability, DS1 was launched. DS1 Ka-band data acquisition activities are expected to start early in 1999.

This article focuses on the antenna efficiency characterization of the DSS-13 BWG antenna using natural radio source observations. The DSS-13 R&D beam-waveguide antenna and system used for the measurements are described in Section 2. The data acquisition technique and model used in the analysis are described in Section 3. The results are presented and discussed in Section 4.

2. Ground Station and Equipment

A series of new antennas for the NASA Deep Space Network (DSN) have been built with the intent of replacing the aging antennas of older designs for deep space communications. These new antennas incorporate a new dual-shape design as well as a beam waveguide (BWG), which utilize a series of additional secondary mirrors to relocate the focal point into a subterranean stationary room located below the main reflector. The advantages of using such a design include increased isolation of the feed package from outside environmental factors such as moisture, wind, and temperature changes and ease of access to the equipment for maintenance, troubleshooting and repair purposes. Figure 1 is a photograph of the DSS-13 beam-waveguide antenna. The beam-waveguide tubing which guides the signal power to the subterranean pedestal room is clearly prominent.

The locations of focal points, mirrors, and feed packages are displayed in the schematic cartoon of Figure 2. The "optical" ray traces of the signals as they propagate are depicted in yellow. The signal energy is collected by the main reflector and subreflector and focused at F1. Reflector mirrors M1 through M4 guide the signal to the rotating ellipsoid focus at F2. The signal is then scattered off the ellipsoid mirror, M5. The X-band signal energy is reflected off the dichroic plate and focused at the other focal point of the ellipsoid mirror and received in the X-band feedhorn package.

The Ka-band signal energy is guided through the beam waveguide in the same manner as the X-band signal, except that after scattering off the ellipsoid, the shorter wavelength Ka-band signal passes through the dichroic plate and is reflected off an additional mirror (M6) mounted in the ceiling and is focused at the other focal point of the ellipsoid and received by the Ka-band feedhorn in the Ka-band package [8].

Figure 3 is a photograph of the center ellipsoid mirror and

several of the surrounding feed packages located in a concentric ring in the subterranean pedestal room. The center ellipsoid mirror can be rotated to select among any of these feed packages, each of which utilizes different frequencies and modes of operation corresponding to its scientific or engineering purpose. Figure 4 is a close-up view of the feed packages used for the X-band and Ka-band experiments discussed in this article.

The ground station can be broken into several subsystems; antenna, microwave, receiver, data acquisition, monitor and control (M&C), and frequency and timing (FTS), each of which will be discussed in the following sub-sections. Figure 5 displays the block diagram of the station configuration used for these experiments.

2.1 Antenna Subsystem

The antenna at K_a-band (17 mdeg HPBW¹) requires more accurate pointing when tracking objects than it does at X-band (63 mdeg HPBW). Whereas an accuracy of 8 mdeg for X-band is sufficient, for K_a-band pointing errors must be kept within 3 mdeg to limit pointing loss to under 0.5 dB. In the past, pointing calibrations had been shown to correct errors to about 5 mdeg RMS in a blind or open-loop mode. Further reduction of pointing errors is realized using an automatic boresight technique which corrects pointing over 5-minute (typical) measurement periods [9].

Typical pointing corrections from this technique, called AUTOBORE, are accurate to within 1 to 2 mdeg RMS. Since pointing corrections are continually updated during successive observations of the same radio source, there is no systematic loss due to beam pointing errors.

Systematic losses due to subreflector focusing and BWG mirror misalignments may be present at some level. These effects are reflected in the measured antenna efficiency versus elevation angle curves which may differ for different radio source declinations.

The overall contribution of the antenna reflectors and BWG mirrors to the noise temperature is about 9.5K at Ka-band and 7 K at X-band.

2.2 Microwave Subsystem

The microwave subsystem takes advantage of the pedestal room layout to allow switching between different feed packages arranged in a ring around a center rotating ellipsoid reflector (see Figure 3). The feed package used for KaAP (see Figure 4) consists of an X/Ka dichroic plate, a 25 dBi horn for X-band, a 26 dBi horn for K_a-band, and high electron mobility transistor (HEMT) low noise amplifiers (LNA) for both bands.

The X/Ka dichroic plate allows simultaneous reception of X-band (8.4 GHz) and Ka-band (32 GHz) signals (see Figures 6a and 6b). The plate passes the higher-frequency Ka-band circularly polarized signals with low insertion loss, while at the same time reflecting the lower-frequency X-band signals. The dichroic plate is a copper

¹ HPBW - Half-Power BeamWidth which is defined as the full-width between the half-power points of the antenna beam

metallic plate (Figure 6a) which is perforated with rectangular apertures (Figure 6b). An oblique angle of incidence is required due to mechanical constraints. A skew grid is employed for bandwidth considerations. The plate employs a 5.08 mm by 5.156 mm rectangular aperture, a 60° skew angle, and a 9.271 mm plate thickness. The elliptical perforated area of the plate is 561.848 by 444.5 mm. The conductivity loss of the rough surface together with the addition to the reflected energy from the horn pattern contributes about 1.3 K to the overall noise temperature at 32.0 GHz. The dichroic plate is described in more detail by Chen et. al. 1993 [10].

The Ka-band feed package includes a 26.1 dBi horn that is an extension of a 22 dBi corrugated horn, followed by a waveguide window. The feedhorn window is composed of kapton. An ellipsoid reflector mirror is located above the 32 GHz feed. The cooled components include a round-to-square transition copper thermal isolator followed by a copper polarizer, a cross-guide coupler, a copper isolator, and a WR-28 copper waveguide going into the LNA. The LNA utilizes four stages of General Electric (GE) and Fujitsu transistors in an amplifier of National Radio Astronomy Observatory (NRAO) design, with a total noise temperature of about 28K.

Compressed helium gas is used to cool the LNA/waveguide feed packages in closed-vessel systems using closed-cycle refrigerators (CCRs). The interior of the housing is kept in a vacuum. The LNAs are cooled by thermally connecting them to the CCR cold station to physical temperatures below 20K, which are thermally stabilized [11].

The loss factor of the cooled waveguide/feed package is estimated to be about 0.325 dB at Ka-band. After adding room temperature contributions due to window and horn, this results in an overall package loss of about 0.4 dB for a noise temperature contribution of about 5K. The resulting estimated temperature of the total package is about 32K, in reasonable agreement with measurements of 34K [11].

At X-band, HEMT devices were also used for the LNA. The LNA and ambient temperature feed components combine for an overall noise temperature contribution of about 28K for the full package.

For 32 GHz, an ambient load is swung over the horn during noise calibrations. For the 8.4 GHz system, a waveguide switch located in front of the LNA is used. Both ambient loads have embedded temperature sensors used to provide data for input to the calibration algorithms. Both systems employ noise diodes which, together with the ambient loads, allow system linearity to be measured (see Sec. 2.4).

The output of the LNAs are connected to an isolator which connects to the bottom plate of the vacuum vessel which in turn connects to the external downconverter assembly which consists of follow up filters and amplifiers.

2.3 Receiver Subsystem

The receiver subsystem used for both frequency bands consists of RF to IF downconverters, an IF switch selector, fiber optics links from the pedestal room to the control room, and an IF distribution assembly in the control room.

The X-band downconversion is performed using an 8.1 GHz first local oscillator (LO). The bandwidth of the second IF filter is 500

MHz.

For K_a-band, two configurations have been used. During the 33.7 GHz data acquisition period (from December 1993 to October 1994), the incoming 33.7 GHz signal was mixed with a 25.2 GHz first LO followed by a 8.2 GHz second LO. The bandwidth of the second IF filter was 100 MHz. For the 32.0 GHz data acquisition system installed in late 1994, the incoming 32.0 GHz signal was mixed with a 23.6 GHz first LO followed by a 8.1 second LO. The bandwidth of the second IF filter was 500 MHz. All LOs are coherent with the station frequency and timing subsystem (FTS).

The downconverter output X-band and Ka-band IF signals are fed into a switch selector, which connects them to the fiber optic system. The IF signals are converted to optical signals, transmitted over fiber optic (FO) links from the pedestal room to the control room where they are converted back to IF. The IF signals are fed to an IF distribution assembly (amplifiers and power dividers), where they are distributed to other subsystems in the control room.

2.4 Data Acquisition Subsystem

The instruments included in this subsystem include the total power radiometer (TPR) used for measuring T_{op} ; the water vapor radiometer (WVR) for measuring atmospheric noise; the weather station; and the data handling terminal (DHT) used for displaying and recording data to disk.

The TPR operates together with the microwave switch controller (USC) to provide calibrated T_{op} measurements during the track. The two incoming IF channels are filtered (20 MHz for X-band and 30 MHz for K_a-band) to limit the incoming noise bandwidth and any RFI. The bandwidth of these filters together with the radiometer integration time (5 sec) define the contribution of the receiver noise for the T_{op} measurements, which lies below 0.01 K for both systems. Variable step attenuators are used to set the power levels to a 1 μ watt level when the LNA input is on the ambient load with noise diode on. Measurements of the total IF noise power are made with two HP8481 power sensors followed by HP437B or HP438A power meters - one each for X-band and K_a-band. The power sensors operate from 10 MHz to 18 GHz within 100 picowatt to 10 μ watt power values. A local computer platform reads these measurements and converts them to T_{op} values, based on the transfer function derived from each calibration.

Calibrations are performed regularly throughout each track alternating with the boresight observations. An initial set of calibrations at zenith is always performed at the beginning of a track (known as a PRECAL) and sometimes at the end of a track (known as a POSTCAL). During each calibration, the TPR measures the total IF noise power while the HEMT input is switched from 1) sky, to 2) sky plus noise diode, to 3) ambient load, to 4) ambient load plus noise diode. The measurements are converted into a transfer function (T_{op} versus total noise power) and also allow for the correction of any non-linearity which may be present. A detailed discussion of the system calibration methodology is presented by Stelzried and Klein 1994 [12].

The WVR, is a small stand alone microwave radiometer package

positioned near the antenna which measures the noise temperature contribution of water in the atmosphere in vapor and liquid form [13]. The WVR measures sky temperatures at 20.7 GHz and 31.4 GHz over effective bandwidths of 320 MHz. It consists of a platform with a small feedhorn and mirror assembly that can observe any point in the sky with a beamwidth of 7°. Comparisons of WVR derived atmospheric noise temperatures with those derived from BWG TPR data have yielded consistent results [14].

A "weather system" samples and records a range of meteorological parameters including atmospheric pressure, air temperature, relative humidity, wind speed, and wind direction. These measurements are input to a program which estimates atmospheric noise temperature and attenuation based on a surface model.

2.5 Monitor and Control Subsystem

All of the subsystems are linked together into an operational system with a high degree of flexibility known as the Monitor and Control (M&C) subsystem. Data have been acquired using M&C systems which ran on 486 PC and SUN workstation platforms. Interfacing to the other subsystems is provided by the local area network (LAN).

2.6 Frequency and Timing Subsystem

For frequency and timing, all of the sensitive reference frequency distributions are made using optical fiber. Optical fiber is also used in the transmission of the broadband IF signals from the pedestal room to the control room. Fiber optics have improved stability over that of coaxial cable.

3. DATA ACQUISITION AND ANALYSIS

Since the KaAP data acquisition began in December 1993 after the end of the Mars Observer KaBLE experiment, the antenna efficiency measurements were acquired on a routine basis. Each time a configuration change was implemented, the performance determined from the new set of measurements was compared with that of the previous configuration. Any resulting change in antenna efficiency was compared with available predictions.

The efficiency measurements were acquired using the receivers located in the subterranean pedestal room of DSS-13 where the incident energy was channeled from the antenna's main reflector and subreflector using a series of beam waveguide and mirrors. In the pedestal room, the feed position consisted of equipment for receiving two simultaneous wavelengths, one at 8.425-GHz (X-band) and one at 32.0-GHz/33.7-GHz (Ka-band), as described in Sec. 2. The observation strategy, the model used to process the data, the observed radio sources and estimated uncertainties will be described here.

3.1 Description of Measurement Sequence

KaAP uses dual frequency observations of natural calibrator radio sources at Ka-band (33.7 GHz and 32.0 GHz) and X-band (8.425 GHz), producing estimates of the antenna efficiency at each frequency. Each track or experiment consists of a series of radio source observations distributed over different parts of the sky over a wide elevation angle range. There were typically one to two tracks

per month, with each lasting 8 to 24 hours in duration. Each track consists of 1) a series of boresight observations of different radio sources, 2) a series of radiometer calibrations, and 3) tipping curves (measurements of cold-sky temperature versus elevation angle from zenith to near horizon). The boresight observations alternate with the calibrations during the main body of the pass, with tipping curves usually performed at the start of, or end of the pass.

A sequence of an X-band boresight, a Ka-band boresight, and radiometer calibrations at both X-band and Ka-band were performed for each measurement cycle of a source when the KaAP effort first started. Afterwards, the tracks consisted of either Ka-band only, or X-band only boresight observations, alternating with the calibrations.

3.1.1 Boresight Observations

Each boresight observation of a radio source involves stepping the antenna beam across the radio source while taking system operating noise temperature measurements (T_{op}) using the TPR. A peak noise temperature due to the source is estimated by fitting a linearized Gaussian beam model [9], over the T_{op} measurements in two orthogonal directions across the radio source; in cross-elevation (XEL) and in elevation (EL). The model is fit over the a priori on-source point (0 dB), the half-power down (-3 dB) points, and off-source points. The solution yields the peak noise temperature due to the radio source, ΔT_{pk} , an estimate of the half-power beamwidth (θ_{HP}), and an estimate of the pointing correction relative to the accumulated pointing correction just prior to the boresight observation, $\Delta\theta$, in each direction.

The peak source noise temperatures are converted into estimates of antenna efficiency using the radio source's catalogued flux density, and corrections for the angular flux distribution over the antenna beam, estimated atmospheric attenuation (to refer the measurements to zero atmosphere), and any system non-linearity which may be present.

3.1.2 System Calibrations

Radiometer calibrations are routinely conducted to correct for gain changes as the experiment progresses and allow the system non-linearity to be determined. The radiometer calibrations were described in Sec. 2.4.

3.1.3 Tipping Curve Measurements

In addition to the boresight observations and system calibrations, a sequence of tip curve observations is routinely performed to characterize the atmosphere. These provide a means of determining the atmospheric loss factor used to refer the antenna efficiency measurements to zero atmosphere, and the atmospheric noise temperature used for statistical cross-comparisons with independent WVR and surface model estimates.

The tipping curves were usually done at the start or end of a pass, with each lasting about 30 minutes. The tipping curve acquisition consists of a set of cold-sky T_{op} measurements at

elevation angles which ranged from near horizon to zenith. Normally, the atmosphere is sampled from 1 airmass (zenith) to about 4 airmasses (14.5° elevation angle).

3.2 Description of Antenna Efficiency Model

Given a radio source of known flux density, the increase in system operating noise system temperature (T_{op}) as determined by the boresight measurements (peak source noise temperature fit over a linearized Gaussian model) is a measure of the antenna efficiency. The antenna efficiency measurement for the BWG antenna is referenced at the plane where the ambient load is inserted during calibrations. This measurement accounts for power losses of the main reflector, subreflector, BWG mirrors, dichroic plate, and any feed package loss including waveguide up to the ambient load plane. For X-band, the antenna efficiency is referred to the input of the HEMT where an ambient load is inserted by a waveguide switch during calibrations. For K_a-band, the antenna efficiency is referred to the input of the feedhorn where an ambient load is swung over it during calibrations.

Given one received component of a randomly polarized radio source, the flux density is given by

$$S = \frac{2 k \Delta T C_r C_p}{A_e} \quad (1)$$

where S = radio source flux density, W/(m²-Hz)
 ΔT = radio source noise temperature increase one would measure in a vacuum (K)
 A_e = effective area of antenna, (m²)
 C_r = source size correction
 C_p = pointing correction
 k = Boltzmann's constant (1.38062 X 10⁻²³ W/(K-Hz))

The source size correction, C_r , accounts for extended structure over the antenna beam, and is equal to 1.0 for a point source. A standard unit for flux density, S , is the Jansky (Jy) (1 Jy = 10⁻²⁶ W/m²-Hz). The pointing correction, C_p , is equal to 1.0 when there is no mispointing.

The AUTOBORE program performs sequential cross-elevation (XEL) and elevation (EL) cuts of a radio source. The measured increases in system operating noise temperature due to a radio source are ΔT_{XEL} and ΔT_{EL} in the cross-elevation and elevation directions, respectively.

The best estimate of the source noise temperature increase, ΔT_m , is the average

$$\Delta T_m = \frac{\Delta T_{xel} + \Delta T_{el}}{2} \quad (2)$$

In order to estimate the antenna efficiency one would measure in a vacuum, the source noise temperature measurements, ΔT_m , are corrected by the atmospheric loss factor, $L_{atm}(\theta)$. The tipping curve

data were used to determine $L_{atm}(\theta)$. Hence, ΔT is estimated from ΔT_m (Eq. (2)) using

$$\Delta T = L_{atm}(\theta) F_{lin} \Delta T_m \quad (3)$$

where F_{lin} is the system linearity factor determined from the radiometer calibration data. For Goldstone, typical zenith values of attenuation, $10\log(L_{atm})$, as determined by the tip curve measurements are 0.035 dB at X-band and 0.15 dB at Ka-band.

Given that the effective area of the antenna is related to the antenna efficiency, ϵ , and antenna diameter, D (m), by

$$A_e = \frac{\epsilon \pi D^2}{4} \quad (4)$$

we can relate ϵ to the other parameters by combining Eqs. (1), (3) and (4) as follows

$$\epsilon = \frac{8 k \Delta T C_r C_p}{S \pi D^2} \quad (5)$$

Another measure of antenna performance is the figure-of-merit, G/T_{op} , or effective gain of the antenna, G , divided by system operating noise temperature, T_{op} . Since G/T_{op} is used for spacecraft-to-ground link studies, the effects of the atmospheric loss are included so that variations over a wide range of atmospheric conditions can be studied.

The effective gain, G , is related to ϵ by

$$G = \frac{\epsilon}{L_{atm}} \left(\frac{\pi D}{\lambda} \right)^2 \quad (6)$$

where D is the antenna diameter (m) and λ is the observing wavelength (m). Therefore,

$$\frac{G}{T_{op}}(\theta) = \frac{\epsilon(\theta) \pi^2 D^2}{L_{atm}(\theta) T_{op}(\theta) \lambda^2} \quad (7)$$

T_{op} includes all contributions seen by the antenna (including cosmic, atmosphere, main structure and mirrors, feed package, amplifier and follow-on equipment). Typical zenith values of T_{op} at the KaAP feed position were 40K at 8.4 GHz and 55K at 32 GHz.

3.3 Radio Source Calibrators

The flux densities, their uncertainties, and the source-size correction factors of the observed natural radio sources have been derived from independent studies and are listed in Table 1. The 8.4 and 32 GHz values for 3C274 and DR21 are from Richter 1994 [15], and the values given for the variable source 3C84 are nominal baseline

where

$$Q = 2 \frac{\sqrt{R_{eq} R_{pol}}}{\rho \theta_{HP}} \quad (10)$$

and where θ_{HP} is the half-power beamwidth of the antenna in radians and R_{eq} and R_{pol} are the equatorial and polar radii of the planet, respectively. For Venus, $R_{eq}=R_{pol}=6120$ km. For Jupiter, $R_{eq}=71492$ km and $R_{pol}=66854$ km.

Table 2
Brightness Temperatures of the Planets

Planet	Frequency (GHz)	T_B (K)	σ_{TB}/T_B (%)	Ref.
Venus	8.4	652	2.3	[16]
	32.0	467	4	[16]
	33.7	461	4	[16]
Jupiter	8.4	210	4	[17]
	32.0	154	5	See text
	33.7	152	5	See note ⁴

The K_a-band brightness temperatures for Venus in Table 2 were extrapolated from a spectral curve given in Steffes, Klein and Jenkins 1990 [16]. For Jupiter, an appropriate blackbody correction was applied to the 33.7 GHz 152K value at 33.7 GHz to get 154K at 32.0 GHz.

Because of larger measurement discrepancies relative to 3C274, the planets have not been routinely observed as calibration sources. Earlier observations of Venus and Jupiter are discussed in Sec. 4.

3.4 Antenna Efficiency Error Contributions

The uncertainty in the antenna efficiency measurements can be estimated using

$$\sigma_e(\theta) = \varepsilon(\theta) \sqrt{\left(\frac{\sigma_S}{S}\right)^2 + \left(\frac{\sigma_{\Delta T_m}}{\Delta T_m}\right)^2 + \left(\frac{\sigma_{L_{atm}(\theta)}}{L_{atm}(\theta)}\right)^2 + \left(\frac{\sigma_{C_p}}{C_p}\right)^2} \quad (11)$$

where

σ_S/S is the uncertainty of the source flux density

$\sigma_{\Delta T_m}/\Delta T_m$ is the uncertainty of the source noise temperature measurement

$\sigma_{L_{atm}}/L_{atm}$ is the uncertainty of the atmospheric loss factor

σ_{C_p}/C_p is the uncertainty due to any mispointing

⁴ M. Gatti, and M. Klein, personal communication, Jet Propulsion Laboratory, Pasadena, California, June 1994.

The values of σ_s/S are given in Table 1 for the extragalactic radio sources and can be inferred from σ_{TB}/T_B in Table 2 for the planets. This contribution defines the absolute calibration error for the measurements.

The uncertainty $\sigma_{\Delta T_m}$ is an estimate of the noise temperature measured by the radiometer during the measurement period. Typical uncertainties for 3C274 at K_a-band are about 0.1 K ($\Delta T_m \sim 2.3K$). The main contributors are expected to be gain instability and atmospheric noise during the AUTOBORE measurement period. This term dominates the observed scatter of the measurements during a pass.

The atmospheric loss factor uncertainty, $\sigma_{L_{atm}}$, can be estimated from the expected variation of the atmospheric noise temperature over a pass. Because the tip curves are usually performed once per pass (not during the AUTOBORE measurements), L_{atm} is effectively a nominal estimate over the pass. Long-term variations in atmospheric attenuation over a pass thus define $\sigma_{L_{atm}}$, while short-term variations (within the period of the boresight measurement) would be manifested in $\sigma_{\Delta T_m}$.

Losses due to beam-pointing errors, σ_{cp} , are expected to be small since AUTOBORE is continually updating the pointing corrections. It is possible that errors due to mispointing may be as high as 0.5%, which still lie below those attributed to radiometer and atmospheric noise. Systematic losses due to errors in subreflector focusing and beam-waveguide mirror misalignments will be reflected directly in the antenna efficiency measurements. Data acquired at other feed positions may have different peak efficiencies and elevation dependent curve shapes because of such misalignments.

4. RESULTS

Figure 7 displays the measured antenna efficiencies at X-band and K_a-band versus elevation angle for data acquired from February to November 1995 at the KaAP X/K_a-band feed position. The X-band data will be discussed in 4.1 and the K_a-band data will be discussed in 4.2. Also discussed will be G/T performance (Sec. 4.3) and a history of DSS-13 K_a-band performance improvements (Sec. 4.4).

The antenna efficiency measurements, Eq. (5), gathered from different radio sources, and different passes for a given frequency band, and station configuration are combined into a common data set. An antenna efficiency versus elevation angle curve is then least-squares fit to the data using a second-degree polynomial model

$$\varepsilon(\theta) = c_0 + c_1 \theta + c_2 \theta^2 \quad (12)$$

where the c_i , $i=1,2,3$ are the solve-for coefficients and θ is the elevation angle of the observation.

Table 3 lists the fitted coefficients of a second degree polynomial using Eq. (12) over the X-band and Ka-band data referenced to the F3 focal point (see Figure 2).

Table 3
Best-fit 2nd Degree Polynomial Coefficients
for DSS-13 X-band and K_a-band Efficiencies
(at F3, no atmosphere)

	C ₀	C ₁	C ₂	ε _{pk} (%)	θ _{pk} (deg)	
X-band	0.675662	0.0019537	-0.000026679	71.1	36.6	All Data
K _a -band	0.344228	0.0111526	-0.000136727	57.1	40.8	3C274
"	0.378161	0.0085412	-0.000097117	56.3	44.4	3C84
"	0.409153	0.0075158	-0.000091870	56.2	41.1	All Data

4.1 Antenna Efficiency Measurements: X-band at F3

Provided in Figure 7 are the data points with estimates of the error bars (excluding the absolute error contribution of the flux density), and the best fit curve for X-band data acquired between February through May 1995. The rms error of the data points about the best-fit curve is 0.9% over 77 observations. The measured peak antenna efficiency is 71.1% at 37° elevation which is in agreement with the 71.8% predicted value based on estimates of individual contributors [18].

A comparison of the measured KaAP X-band antenna efficiency was in good agreement with that measured at another X-band feed system at DSS-13 by Imbriale, Esquivel and Manshadi 1995 [8]. After backing out estimated contributions of the feed packages, the X-band efficiencies referred to common antenna hardware were 75.5% at the S/X feed position and 75.9% at the KaAP feed position.

The X-band brightness temperatures of the planets Jupiter and Venus in Table 2 produced results (using earlier 1994 data) which were in reasonable agreement with those of 3C274. The peak X-band antenna efficiency using Venus-only data was 2.1% lower than that of the 3C274-only data, but still within the 2.3% uncertainty given in Table 2. The X-band antenna efficiency using Jupiter-only data was within 0.1% of the efficiency computed using 3C274-only data.

4.2 Antenna Efficiency Measurements: K_a-band at F3

Figure 7 also displays the antenna efficiency at 32.0 GHz (K_a-band) versus elevation angle in the form of the data points with estimated error bars (excluding the absolute error contribution in flux density), and the best fit curve over the data acquired from February to November 1995. The RMS of the data points about the best-fit curve is 1.9% over 444 total observations. The measured peak antenna efficiency of the 3C274-only data points (321 observations) is 57.1% at 40.8° elevation which is in agreement with the 56.7% predicted value based on independent estimates of individual contributors. The measured peak antenna efficiency for earlier data acquired at the 33.7 GHz KaBLE frequency (52.2%) is also in agreement with its predicted value (52.1%) [18].

Figure 8 displays the K_a-band data along with the 3C274 and the 3C84 best fit curves. The northern-passing 3C84 high-elevation angle antenna efficiency measurements (maximum elevation of 84°) lie above those of 3C274 (maximum elevation of 67.2°). For the KaAP feed

position in the DSS-13 pedestal room, the antenna efficiency is higher for sources with declinations greater than 35° which rise and set in the north. The increased spread in the data between sources is attributed to a dependence in the antenna efficiency due to probable misalignments in the beam-waveguide mirrors. This behavior is similar to that noted by Alvarez et. al. 1995 [19] for K_a -band measurements acquired at another BWG antenna located in the Goldstone complex.

The measured K_a -band efficiencies show no significant variation with azimuth after removing the elevation angle dependence from the data. This is consistent with the conclusion noted by other investigators [8].

The radio sources used for the K_a -band antenna efficiency determination discussed above were the primary calibrator 3C274 and the variable source 3C84 (used primarily for curve shape). The planets Venus and Jupiter were observed for several passes performed during earlier 33.7 GHz sessions. The peak antenna efficiency of the Venus data using $T_B=461K$ in Table 2 was 7.3% below that of the 3C274 data. If the peak antenna efficiency using Venus data is scaled to match that of 3C274 data, the resulting $T_B=430K$ still lies within the $1-\sigma$ uncertainty of the Steffes et. al. 1990 emission spectrum [16]. Possible contributions to this discrepancy include errors in the relative flux calibration of Venus and 3C274, errors due to significant brightness temperature variation with phase angle (del Ciampo 1989) [20], and modeling uncertainty in estimating the source size correction of a planet. For the Jupiter data, using T_B given in Table 2, the estimated peak antenna efficiency was 1.5% below that using 3C274 data, which is within the 5% quoted uncertainty.

The gravity induced roll-off of the antenna efficiency curve extrapolated to a 6.6° elevation angle (33.8° below the elevation angle of peak antenna efficiency) shows a projected degradation of about 1.4 dB (using 3C274 data). Holography performed at 46.5° and 12.7° elevation predicts a 2 dB degradation between these two points. The estimated 1.4 dB degradation of the KaAP curve is consistent with the 2 dB holographic prediction as there is a large uncertainty in extrapolating the (3C274 only) KaAP curve to an elevation angle (6.64°) where there are no data. At 20° elevation, the estimated 52.8% antenna efficiency corresponds to a degradation of 0.35 dB relative to the peak 57.2% value.

During certain passes, anomalous data points were observed 1) when the measured wind speeds exceeded 20 mph and the antenna was pointed directly into the direction of the oncoming wind or, 2) when the wind speed exceeded 30 mph. The majority of these data points were automatically removed due to the magnitude of the AUTOBORE pointing offsets exceeding a set 2 mdeg tolerance. Cases where the pointing errors were acceptable but the measured efficiencies were suspect occurred during periods of significant gain variations and were thus deleted. A possible cause of the large gain variations is insufficient isolation of the pedestal room environment from significant outside weather changes. Data from passes which occurred during especially turbulent weather including periods of rain have also been removed due to the breakdown of the boresight algorithm in

response to the large atmospheric variations in T_{op} .

The rms scatter of the data about the fitted polynomials provides a measure of the noise in the data. For 3C274-only data, the rms scatter (1.6%) agrees well with that of 3C84-only data (1.7%). The major contributors to this scatter are expected to be radiometer gain instability, atmospheric noise variations, and error in determination of the atmospheric loss factors used to refer the measurements to zero atmosphere. Measured values of gain instability from radiometer calibration data are consistent with the 1.0% rms scatter of data acquired from a single source during a single pass suggesting that radiometer gain fluctuation is the dominant error source during these "good" weather passes.

The higher amount of scatter for the full data set combined over the several different passes, 1.6%, is likely due to differences in how accurately the atmospheric loss corrections, L_{atm} , can be determined from one pass to the next. The atmospheric loss factor is usually determined from a single tip curve measurement, either at the start or end of a pass.

4.3 G/T_{op} Performance

The G/T_{op} figure-of-merit characterizes the ground station contribution used in link studies by spacecraft mission planners. Figure 9 is the G/T_{op} estimated from the data at both frequencies using Eq. (7). The relative link advantage of K_a -band over X-band plotted in Figure 10 is the K_a -band G/T_{op} data point in Figure 9 differenced from the fit value over the X-band data points at the observed K_a -band data point elevation angle. From Figure 10, we see a 7 to 9 dB advantage of K_a -band relative to X-band for the current station configuration. However, if both K_a -band and X-band G/T_{op} measurements are adjusted using projected noise temperatures of improved HEMT LNAs⁵, the resulting ground link advantage lies between the expected 6 to 8 dB.

4.4 History of DSS-13 BWG Performance Improvements at K_a -band

Since the DSS-13 BWG antenna was first placed into operation in 1990, a series of performance improvements have been implemented. Figure 11 displays each curve which was fit from the measured K_a -band antenna efficiency data acquired between these configuration changes. Note the progressive improvement in peak antenna efficiency as each configuration change was implemented.

Curve A in Figure 11 is the antenna efficiency curve measured in January 1991 during DSS-13's first configuration at 32 GHz as part of its post-construction performance evaluation [21]. The data for this curve were acquired using a test package located at a different F3 feed position in the DSS-13 pedestal room. Initial theodolite and holography panel setting sessions were conducted in Aug-Sep 1990, resulting in 0.42 mm normal rms surface error of the main reflector⁶.

⁵ J. Shell, personal communication, Jet Propulsion Laboratory, Pasadena, California, June 12, 1995. $T_{lna}(X)=6K$; $T_{lna}(K_a)=13K$.

⁶ D. Rochblatt, J. Withington, B. Seidel, and H. Jackson, "Performance Improvement of DSS-13 at the Rigging Angle by Unbending the Panels in Rings 8 and

In January 1992, the panels were readjusted with a resulting normal rms surface error of 0.38 mm. Other activities which occurred during the interim between curves A and B was the stiffening of the turntable platform of the ellipsoid mirror in the pedestal room used to direct the incoming RF energy to the desired feed position, and the removal of a bypass feed shroud which was used for early testing of the antenna.

The first KaAP sessions were conducted between December 1993 and January 1994 at the KaBLE frequency of 33.7 GHz. These data produced a peak measured antenna efficiency of 48.8% at 59.5° elevation (curve B). The net improvement of the curve B peak efficiency over that of curve A was found to be consistent with the expected improvement after taking into account all known configuration differences between the two sessions. However, as seen in Figure 11, curve B is peaked significantly away from the 45° rigging angle at about 60°. This have been caused by the stiffening of the ellipsoid support structure with no followup mirror alignment activity.

The January-February 1994 holography session included adjustment of the panels in the outer two rings of the main reflector, resulting in an improved normal rms surface error of 0.31 mm. In addition, a series of mirror alignment operations⁷ were conducted to move the peak of the antenna efficiency curve nearer 45°. This next series of measurements (curve C) (Feb-Sept 1994) yielded a peak antenna efficiency of 50.1% at an elevation angle of 39.5°.

In September 1994, a manual adjustment in the subreflector lateral X-position of 0.2" was made. A small data set conducted shortly after showed a small improvement with a peak antenna efficiency of 52.2% at 45.4° (curve D).

In October 1994, the KaAP K_a-band system was modified to receive the standard DSN allocated frequency band at 32.0 GHz (replacing the KaBLE 33.7 GHz system). At the same time, additional subreflector lateral X-position adjustments were made and a new subreflector look-up table was installed. The resulting November-December 1994 data set at 32.0 GHz showed an improved peak antenna efficiency of 54.3% at 48.4° elevation angle, but with a significantly flattened curve (curve E). The expected improvement in peak antenna efficiency at 32.0 GHz should have been significantly greater (with the same curve shape). It was found that the subreflector optimization procedures using low-resolution holography had been performed at another feed position in the pedestal room at DSS-13. Upon checking the ellipsoid and subreflector at the KaAP position using radiometry, it was found that a significant additional 0.05" subreflector Z-position correction was required to increase the peak antenna efficiency⁸. The most recent

⁹", JPL IOM 3328-94-023 (JPL internal document), March 23, 1994.

⁷ R. Thomas, "DSS 13 Mirror Alignment", Planning Research Corporation Inc. memorandum, February 18, 1994.

⁸ V. Vilnrotter, personal communication, Jet Propulsion Laboratory, Pasadena, California, January 1995.

data set (curve F in Figure 11) presented and discussed in section 4.2 displays the improvement over curve E after applying this correction. The peak antenna efficiency of 57.1% occurs at 40.6° elevation angle. The measured improvement of 0.2 dB is consistent with the 0.14 dB improvement predicted from holography⁹.

In late 1996, the HEMT Ka-band package was removed from the feed position and other packages were installed for testing and demonstration purposes. Since February 1997, a monopulse receiver has been in place routinely acquiring KaAP natural radio source and Mars Global Surveyor (MGS) KaBLE-II spacecraft Ka-band data [6,7].

5. CONCLUSION

The KaAP antenna efficiency measurements acquired at the DSS-13 R&D beam waveguide (BWG) antenna conducted between December 1993 and November 1995 have been presented. This on-going effort has continued in order to characterize the antenna efficiency performance and Ka-band-over-X-band link advantage, and to supplement measurements acquired from spacecraft signals.

ACKNOWLEDGEMENTS

I would like to thank W. Imbriale, J. Layland, R. Clauss, C. Stelzried, C. Edwards, D. Rochblatt, D. Bathker, and M. Klein for many informative discussions and comments; the DSS-13 station personnel for conducting the experiments and acquiring the data (G. Bury, C. Goodson, L. Smith, G. Farner, R. Reese, R. Littlefair, J. Crook, J. Garnica, L. Skjerve and L. Tanida; E. Paulsen, M. Britcliffe, J. Bowen, V. Vilmrotter and S. Stewart for providing information on equipment and station specifications; and T. Rebold for assistance in software development. The research described in this paper was carried out by the Jet Propulsion Laboratory, California Institute of Technology, under a contract with the National Aeronautics and Space Administration.

REFERENCES:

- [1] J. W. Layland and L. L. Rauch, "The Evolution of Technology in the Deep Space Network: A History of the Advanced Systems Program", The Telecommunications and Data Acquisition Progress Report 42-130, vol. April - June 1996, Jet Propulsion Laboratory, Pasadena, California, pp. 96-103, August 15, 1997.
- [2] J. G. Smith "Ka-Band (32 GHz) Downlink Capability for Deep Space Communications", The Telecommunications and Data Acquisition Progress Report 42-88, vol. October - December 1986, Jet Propulsion Laboratory, Pasadena, California, pp. 96-103, February 15, 1987.
- [3] J. W. Layland and J. G. Smith, "A Growth Path for Deep Space Communications", The Telecommunications and Data Acquisition Progress Report 42-88, vol. October - December 1986, Jet Propulsion Laboratory, Pasadena, California, pp. 120-125, February 15, 1987.

⁹ D. Rochblatt, personal communication, Jet Propulsion Laboratory, Pasadena, California, March 17, 1995.

- [4] A. L. Riley, D. M., Hanson, A. Mileant, and R. W. Hartop, "A Ka-Band Beacon Link Experiment (KABLE) with Mars Observer", The Telecommunications and Data Acquisition Progress Report 42-88, vol. October - December 1986, Jet Propulsion Laboratory, Pasadena, California, pp. 141-147, February 15, 1987.
- [5] T. A. Rebold, A. Kwok, G. E. Wood, and S. Butman, "The Mars Observer Ka-Band Link Experiment", The Telecommunications and Data Acquisition Progress Report 42-117, vol. January - March 1994, Jet Propulsion Laboratory, Pasadena, California, pp. 250-282, May 15, 1994.
- [6] Morabito, D. D., Butman, S., and Shambayati, S., "Recent Results from the Mars Global Surveyor Ka-band Link Experiment (MGS/KaBLE-II)", Proceedings of the Fourth Ka-Band Utilization Conference, November 2-4, 1998, Venice, Italy. IIC - Istituto Internazionale delle Comunicazioni, Via Perinace - Villa Piaggio, 16125 Genova, Italy, pp. 365-372.
- [7] Butman, S., Morabito, D. D. Mittskus, A., Border, J., Berner, J., Whetsel, C., Gatti, M., Foster, C., Vilnrotter, V., Cooper, H., Del Castillo, A., Kwok, A., Weese, J., Speranza, M., David, R., Adams, W., McMechen, A., Goodson, C., Bury, G., and Reece, D., "The Mars Global Surveyor Ka-Band Link Experiment (MGS/KaBLE-II)", Proceedings of Third Ka-Band Utilization Conference and International Workshop on SCGII, September xx-xx, 1997, Naples, Italy. F. Bertoldi, Istituto Internazionale delle Comunicazioni, Genova, Italy, pp. 179-186.
- [8] W. A. Imbriale, Esquivel, M. S., and F. Manshadi "Novel Solutions to Low-Frequency Problems With Geometrically Designed Beam-Waveguide Systems", The Telecommunications and Data Acquisition Progress Report 42-122, vol. April-June 1995, Jet Propulsion Laboratory, Pasadena, California, pp. 138-150, August 15, 1995.
- [9] L. S. Alvarez, "Analysis and Applications of a General Boresight Algorithm for the DSS-13 Beam Waveguide Antenna", The Telecommunications and Data Acquisition Progress Report 42-111, vol. July - September 1992, Jet Propulsion Laboratory, Pasadena, California, pp. 48-61, November 15, 1992.
- [10] J. C. Chen, P. H. Stanton, and H. F. Reilly, "Performance of the X/Ka-/KaBLE-Band Dichroic Plate in the DSS-13 Beam Waveguide Antenna", The Telecommunications and Data Acquisition Progress Report 42-115, vol. July-September, 1993, Jet Propulsion Laboratory, Pasadena, California, pp. 54-64, November 15, 1993.
- [11] J. Bowen and D. Neff, "A Cryogenic Seven Element HEMT Front End for DSS-13" The Telecommunications and Data Acquisition Progress Report 42-114, vol. April-June, 1993, Jet Propulsion Laboratory, Pasadena, California, pp. 51-60, August 15, 1993.
- [12] C. T. Stelzried, and M. J. Klein, "Precision DSN Radiometer Systems: Impact on Microwave Calibrations", Proc. of the IEEE, vol. 82, pp. 776-787, May 1994.
- [13] S. J. Keihm, "Water Vapor Radiometer Measurements of the Tropospheric Delay Fluctuations at Goldstone Over a Full Year", The Telecommunications and Data Acquisition Progress Report 42-

- 122, vol. April-June 1995, Jet Propulsion Laboratory, Pasadena, California, pp. 1-11, August 15, 1995.
- [14] Morabito, D. D., Clauss, R., and Speranza, M., "Ka-Band Atmospheric Noise-Temperature Measurements at Goldstone, California, Using a 34-Meter Beam-Waveguide Antenna", The Telecommunications and Data Acquisition Progress Report 42-132, October-December 1997, Jet Propulsion Laboratory, Pasadena, California, pp. 121-152, February 15, 1998.
 - [15] P. Richter, "Radio Source List for Antenna Calibration", DSN No. 890-269, Issue Date October 15, 1994, JPL Doc. No. D-3801 (JPL internal document), Jet Propulsion Laboratory, California Institute of Technology.
 - [16] P. G. Steffes, M. J. Klein, and J. M. Jenkins, "Observations of Microwave Emission of Venus from 1.3 to 3.6 cm", *Icarus* 84, 83-92 (1990).
 - [17] I. de Pater, and S. T. Massie, "Models of the Millimeter-Centimeter Spectra of the Giant Planets", *Icarus* 62, 143-171 (1985).
 - [18] D. D. Morabito, "The Efficiency Characterization of the DSS-13 34-Meter Beam-Waveguide Antenna at Ka-Band (32.0 and 33.7 GHz) and X-band (8.4 GHz)", The Telecommunications and Data Acquisition Progress Report 42-125, January-March 1996, Jet Propulsion Laboratory, Pasadena, California, pp. 1-20, May 15, 1996.
 - [19] L. S. Alvarez, M. J. Britcliffe, M. M. Franco, S. R. Stewart, and H. J. Jackson, "The Efficiency Calibration of the DSS-24 34-Meter Diameter Beam-Waveguide Antenna", The Telecommunications and Data Acquisition Progress Report 42-120, vol. October-December 1994, Jet Propulsion Laboratory, Pasadena, California, pp. 174-187, February 15, 1995.
 - [20] L. del Ciampo, "Centimeter Emission Variation of Venus" Masters Dissertation in Space Science/Radioastronomy and Solar Physics, October 1989, Instituto de Pesquisas Espaciais.
 - [21] S. D. Slobin, T. Y. Otoshi, M. J. Britcliffe, L. S. Alvarez, S. R. Stewart, and M. M. Franco, "Efficiency Measurement Techniques for Calibration of a Prototype 34-Meter-Diameter Beam-Waveguide Antenna at 8.45 and 32 GHz", *IEEE Trans. on Microwave Theory and techniques*, Vol. 40, No. 6, June 1992, pp. 1301-1308.

Figure Captions

- 1) Photograph of the 34-m beam waveguide antenna, DSS-13, located at the Goldstone Deep Space Communications Complex, near Barstow, California.
- 2) Geometric configuration diagram of reflectors and mirrors on DSS-13 BWG antenna along with locations of focal points.
- 3) Photograph of interior subterranean pedestal room showing center ellipsoid and surrounding feed-packages.
- 4) Photograph of KaAP X-band and Ka-band feed packages, the X/Ka dichroic plate along with portion of the center ellipsoid mirror.
- 5) Block diagram of DSS-13 station configuration used for the

- experiments.
- 6) Photographs of dichroic plate (a) and close-up of rectangular apertures (b), used for simultaneous reception of X-band and Ka-band signals.
 - 7) Antenna efficiency versus elevation angle of DSS-13 BWG antenna at X-band (8.4 GHz) and Ka-band (32.0 GHz) along with error bars and best-fit curves.
 - 8) Antenna efficiency versus elevation angle of DSS-13 BWG antenna at Ka-band (32.0 GHz) along with best-fit curves for 3C274-only data and 3C84-only data.
 - 9) G/T_{op} figure-of-merit versus elevation angle of DSS-13 BWG antenna at X-band (8.4 GHz) and Ka-band (32.0 GHz).
 - 10) G/T_{op} ground station advantage (Ka-band over X-band) versus elevation angle of DSS-13 BWG antenna.
 - 11) History of Ka-band performance measurements at DSS-13: Ka-band antenna efficiency versus elevation angle.

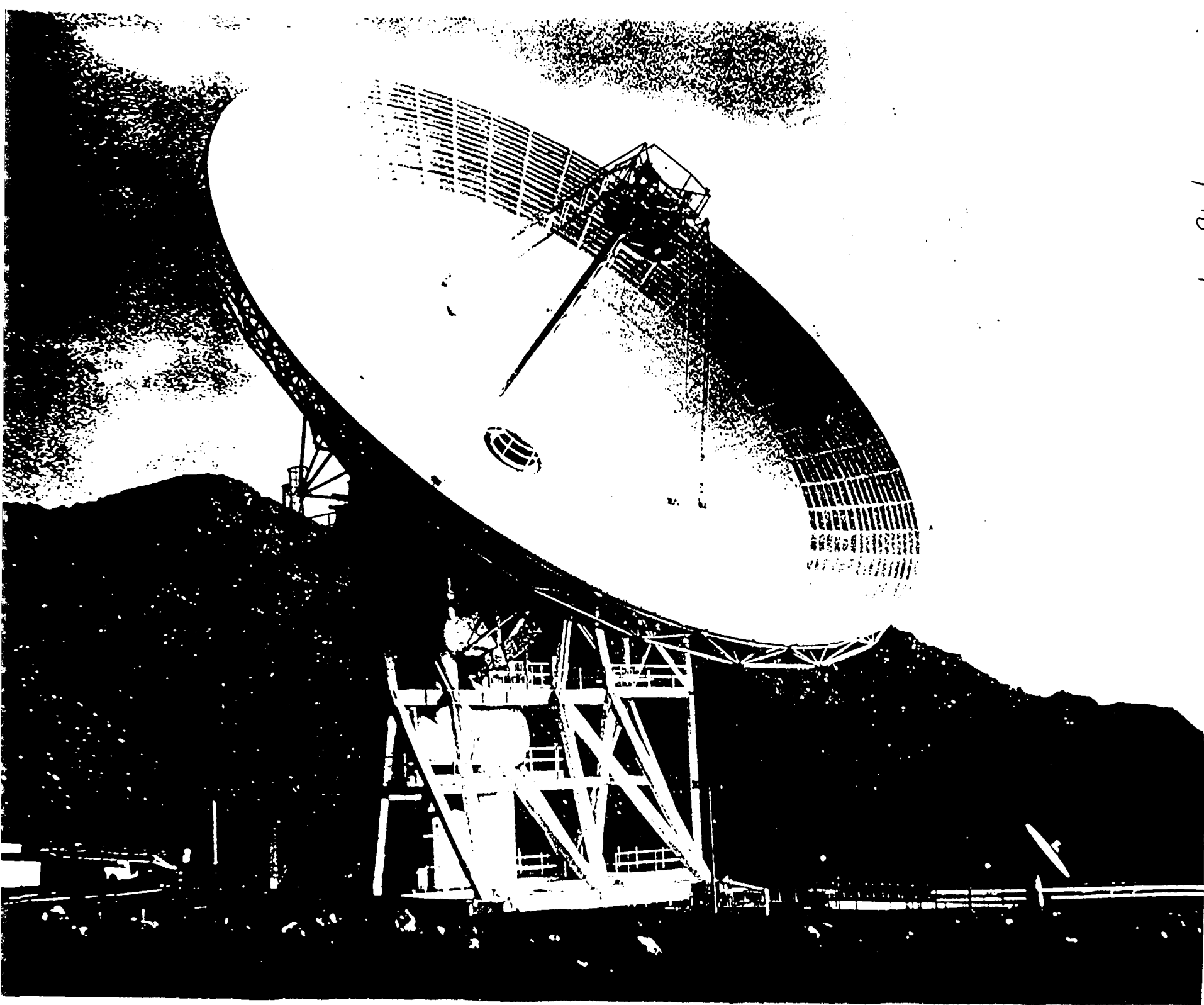
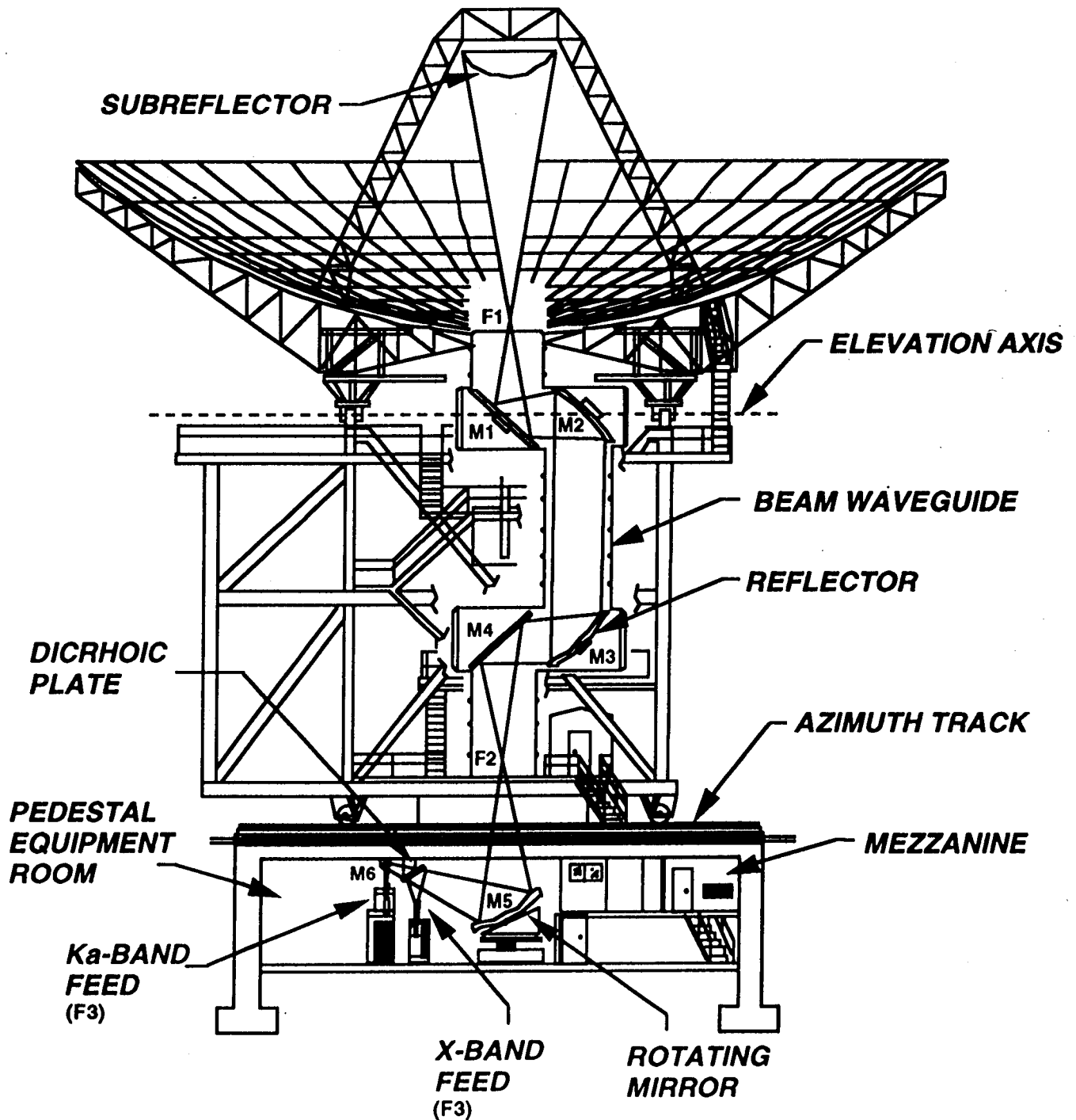


FIG 1

Figure 2



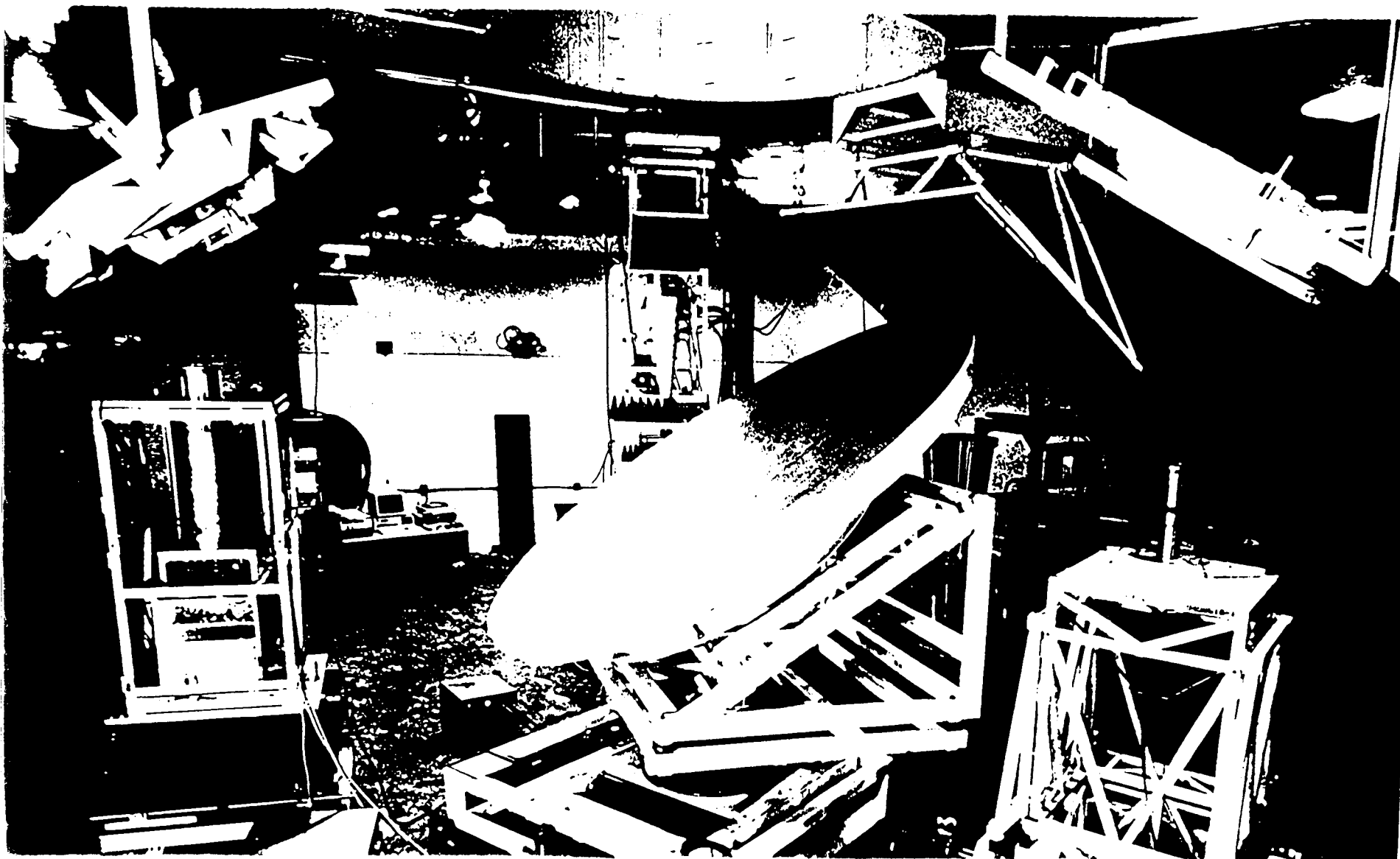


FIG 3

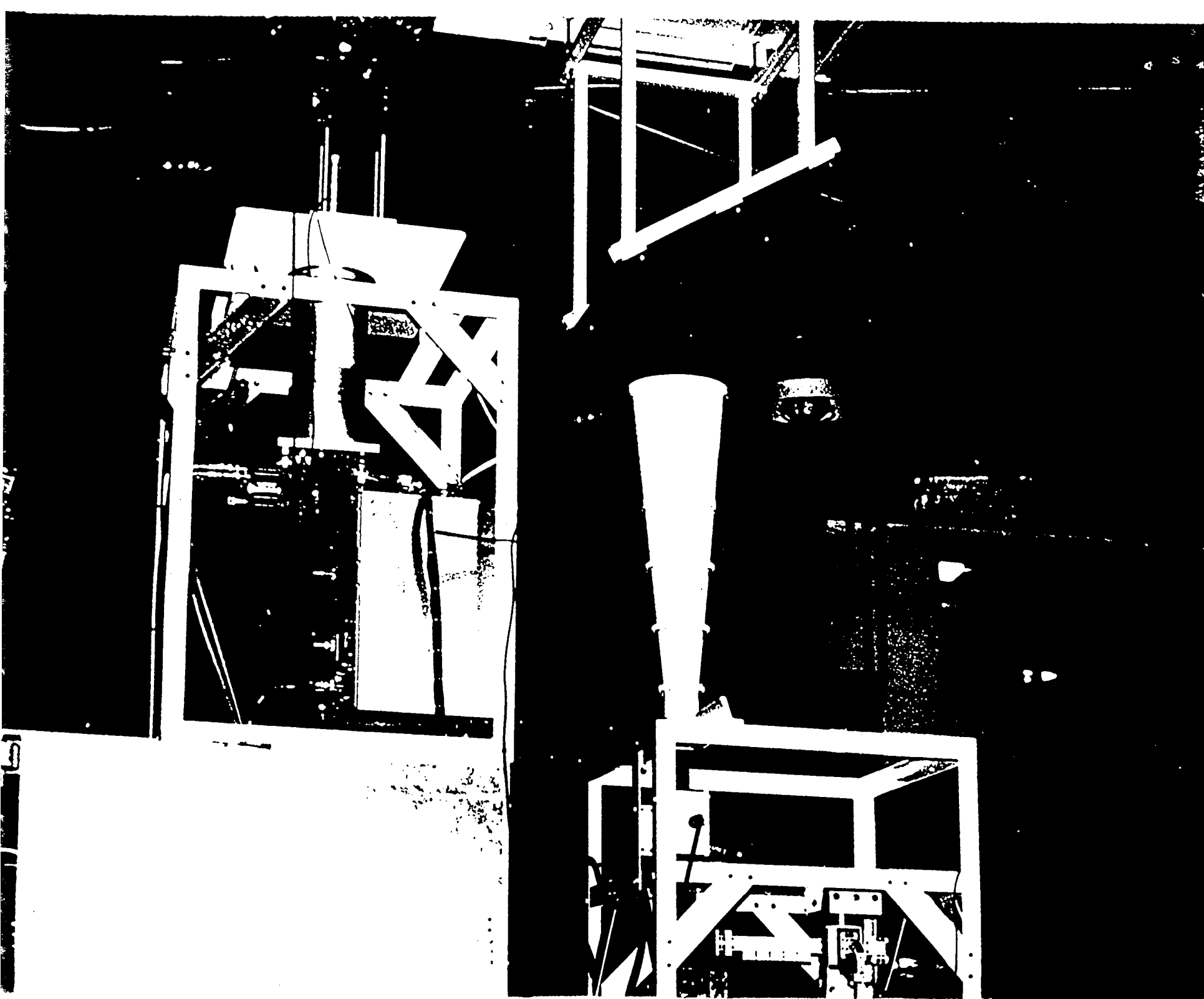


Fig. 47

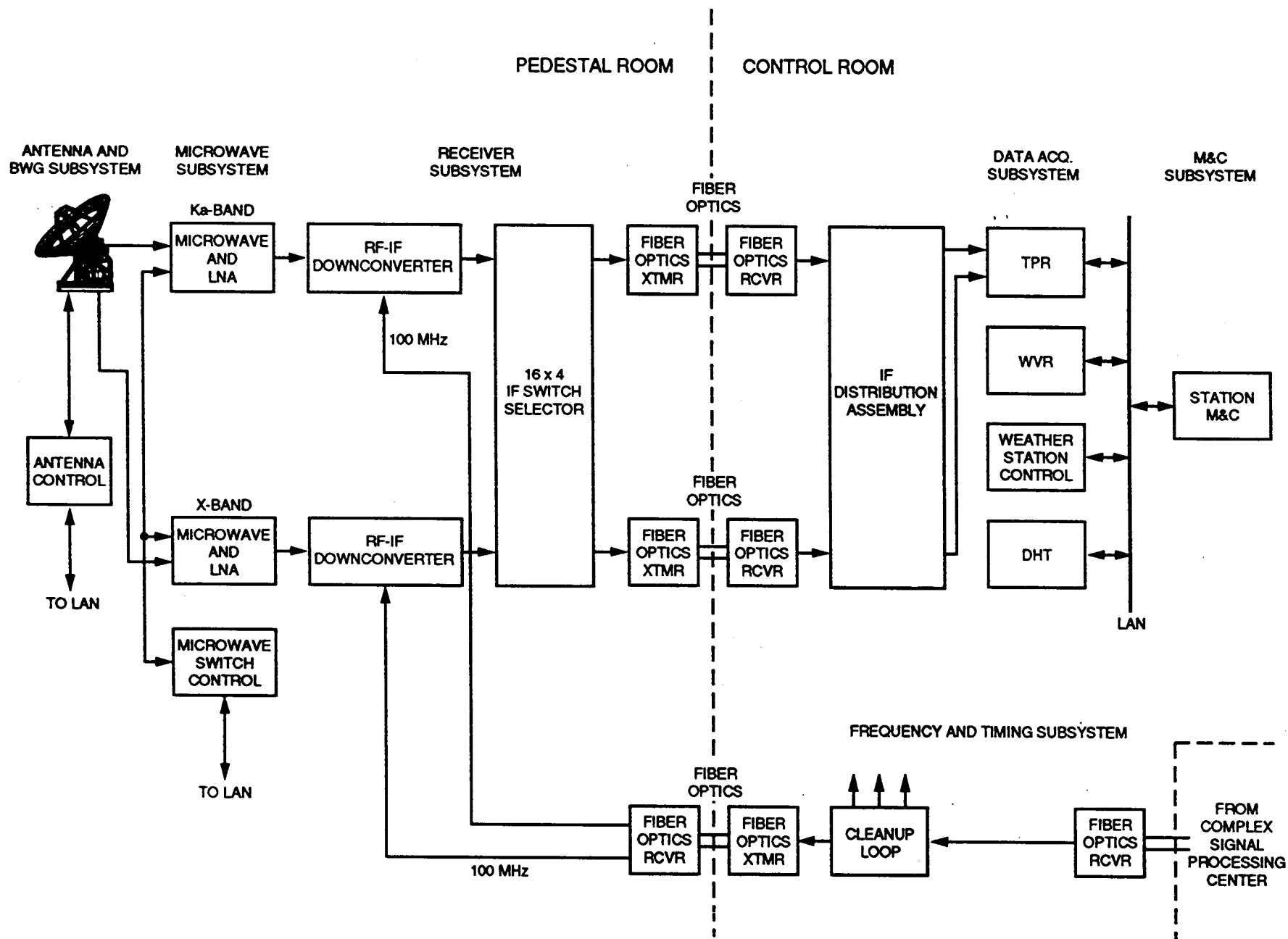
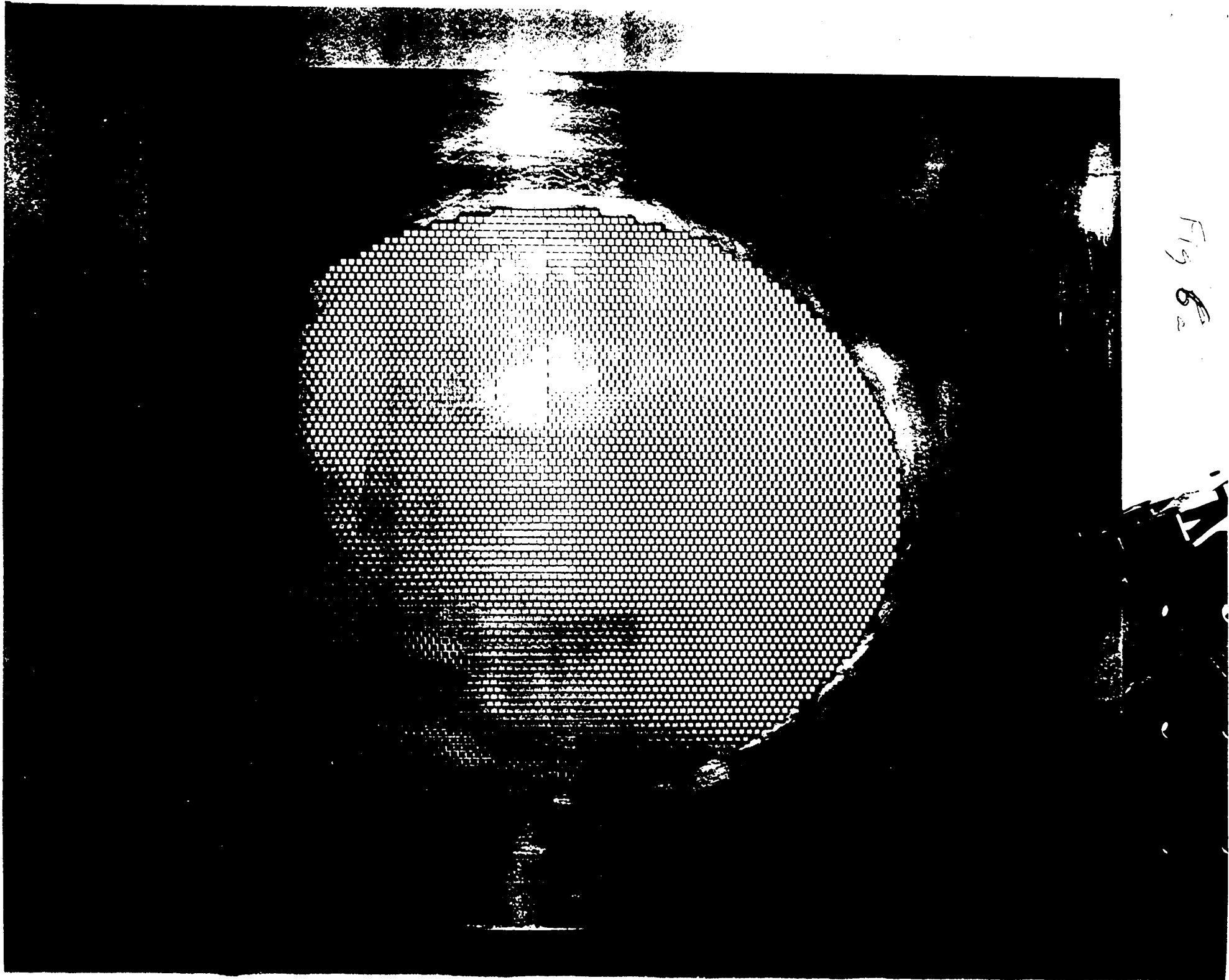


Figure 5



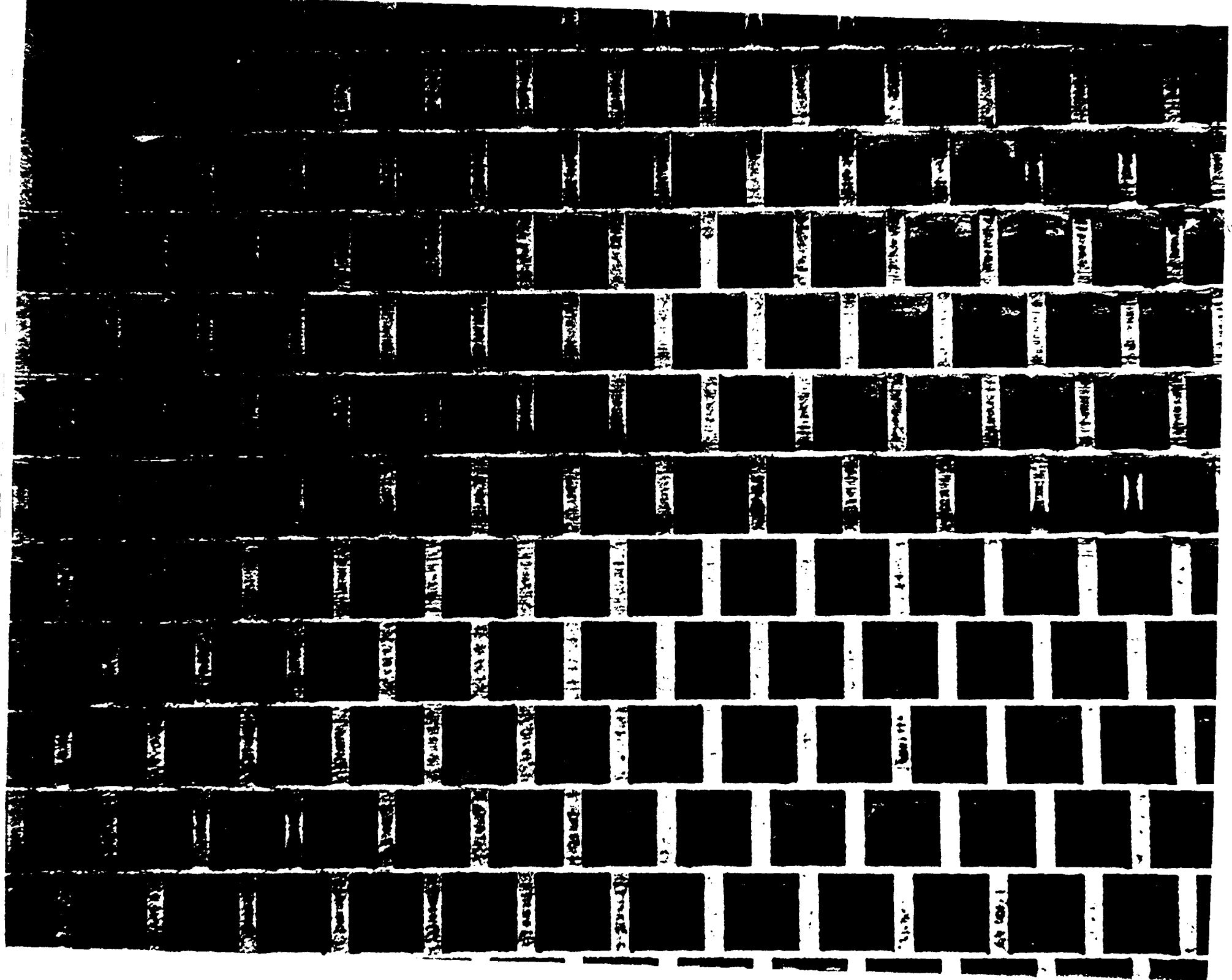


Fig 7

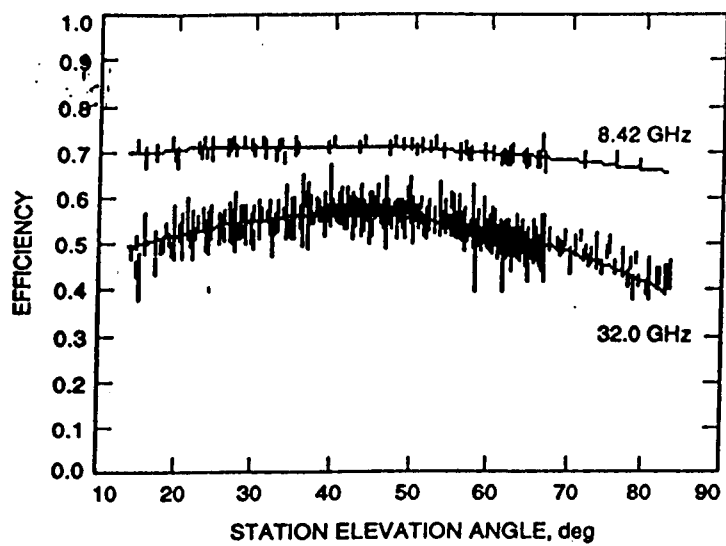


Fig ~~7~~ 8

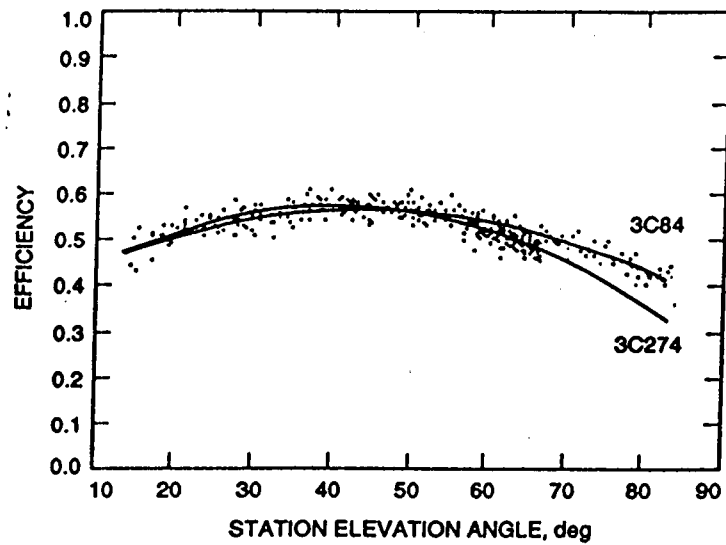


Fig ~~X~~ 9

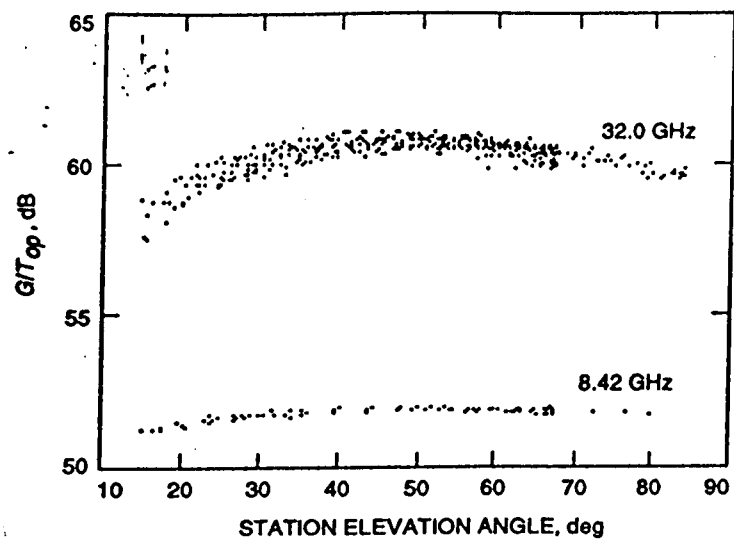


Fig 10

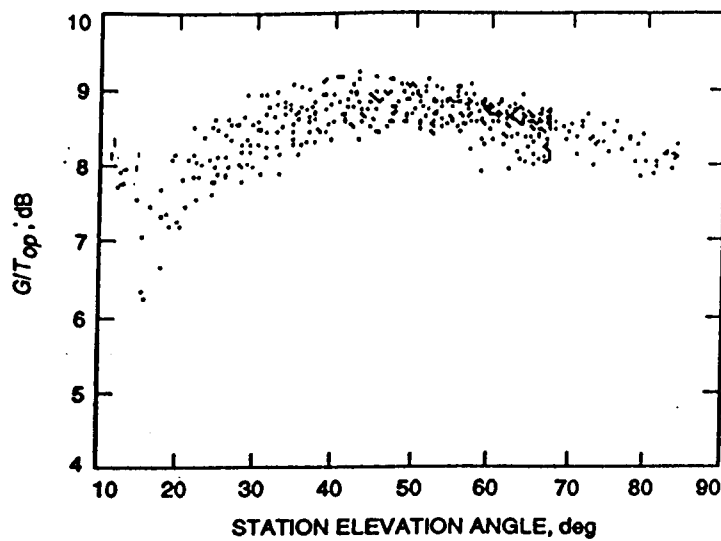


Fig 11

